Epipole-Based Guidance for an Autonomous Glider

Wilson O. Achicanoy[1]
Universidad de Nariño, Pasto 520002, Colombia.

Carlos F. Rodriguez[2]
Universidad de los Andes, Bogotá 111711, Colombia.

Carlos Sagüés[3] and Gonzalo López-Nicolás[4]
Universidad de Zaragoza, Maria de Luna 1 E-50018, España.

Two strategies based on epipolar geometry are proposed to guide an aerial vehicle to a desired position defined by a reference image. The starting point to design the strategies is the engagement geometry of two images: the on-line image provided by the on-board camera and the reference image. A full closed-loop system is derived combining the concept of classical proportional navigation, with the input-output nonlinear control technique, and the tracking of epipolar references. Our main contribution is the definition of a guidance algorithm based on the partial linearization of the full closed-loop system by means of pure image-based information: the epipolar geometry across two views. The proposed formulation avoids the requirement of estimating the range between the current and target positions. Conditions for stability are established for both strategies. Simulation experiments show the interception of the target position by the aerial vehicle and additionally, a simple attitude control.

---

[1] Assistant Professor, Departamento de Electrónica, Universidad de Nariño; wilachic@udenar.edu.co. AIAA Member.
[2] Associate Professor, Departamento de Ingeniería Mecánica; crodrigu@uniandes.edu.co.
[3] Professor, Departamento de Informática e Ingeniería de Sistemas, Instituto de Investigación en Ingeniería de Aragón; csagues@unizar.es.
[4] Associate Professor, Departamento de Informática e Ingeniería de Sistemas, Instituto de Investigación en Ingeniería de Aragón; gonlopez@unizar.es.

Nomenclature

$\mathcal{A}$ $\qquad$ = inertial North-East-Down (NED) coordinate system

${}^{\mathcal{A}}\mathbf{a}$ $\qquad$ = origin of $\mathcal{A}$, m

$\mathcal{B}$ $\qquad$ = body-fixed coordinate system

${}^{\mathcal{A}}\mathbf{b}$ $\qquad$ = origin of $\mathcal{B}$, m

$\mathcal{C}$ $\qquad$ = current camera-fixed coordinate system

${}^{\mathcal{A}}\mathbf{c}$ $\qquad$ = origin of $\mathcal{C}$, m

$\mathcal{T}$ $\qquad$ = target camera-fixed coordinate system

${}^{\mathcal{A}}\mathbf{t}$ $\qquad$ = origin of $\mathcal{T}$, m

μ_c, μ_t $\qquad$ = lead and aspect angles, deg

$\mathcal{CT}$-LoS $\qquad$ = Current-Target Line of Sight, i.e., LoS through the camera centers

λ $\qquad$ = angle of the $\mathcal{CT}$-LoS, deg

$\dot{\lambda}$ $\qquad$ = rate of change of the $\mathcal{CT}$-LoS angle, deg/s

γ_c, γ_t $\qquad$ = flight-path angles of the current and target cameras, deg

f_c, f_t $\qquad$ = focal length of the current and target cameras, pixels

$e_{c,y}$, $e_{t,y}$ $\qquad$ = current and target epipolar coordinates, pixels

$\dot{e}_{c,y}$, $\dot{e}_{t,y}$ $\qquad$ = rate of change of the current and target epipolar coordinates, pixels/s

$r_{c,t}$ $\qquad$ = magnitude of the range between camera centers, m

n $\qquad$ = magnitude of the lateral acceleration perpendicular to the $\mathcal{CT}$-LoS, m/s^2

$\mathcal{CT}$-system = state space representation of the engagement

η $\qquad$ = $[\lambda, \dot{\lambda}]^T$, $\mathcal{CT}$-system's state vector

$\mathbf{A}$ $\qquad$ = $\mathcal{CT}$-system's state matrix

$\mathbf{B}$ $\qquad$ = $\mathcal{CT}$-system's input vector

u $\qquad$ = n, $\mathcal{CT}$-system's input, m/s^2

ξ_i $\qquad$ = $[e_{i,y}, \dot{e}_{i,y}]^T$, linearized output's state vector

$\mathbf{A}_i$ $\qquad$ = linearized output's state matrix

$\mathbf{B}_i$ $\qquad$ = linearized output's input vector

v_i $\qquad$ = linearized output's input, pixels/s^2

$\mathbf{C}_i$ $\qquad$ = linearized output's measurement vector

$\xi_{i,1,r}$ $\qquad$ = $e_{i,y,r}$, epipolar reference, pixels

σ_i $\qquad$ = tracking error, pixels·s

$\mathbf{K}_i$ $\qquad$ = state feedback gain vector

ω_i $\qquad$ = input disturbance, pixels/s^2

$\mathbf{x}_i$ $\qquad$ = $[\xi_i^T, \sigma_i]^T$, closed-loop augmented linearized output's state vector

$\mathbf{A}_{i,a}$ $\qquad$ = closed-loop augmented linearized output's state matrix

$\mathbf{B}_{i,a}$, $\bar{\mathbf{B}}_{i,a}$ = closed-loop augmented linearized output's input vectors

χ_i $\qquad$ = $[\eta^T, \mathbf{x}_i^T]^T$, full closed-loop system's state vector

$f(\chi_i)$ $\qquad$ = full closed-loop system's nominal system

W_i $\qquad$ = full closed-loop system's input perturbation

Subscripts and superscripts:

i $\qquad$ = c: current, t: target

y $\qquad$ = epipolar coordinate in the vertical plane

a $\qquad$ = augmented matrices and vectors

r $\qquad$ = reference epipolar coordinate

$\mathcal{A}$, $\mathcal{B}$, $\mathcal{C}$, $\mathcal{T}$ = relative to respective coordinate frame

I. Introduction

IN the last years, the proliferation of unmanned aerial vehicles for several purposes (monitoring, delivery, recreation, etc.), has promoted the development of Guidance, Navigation and Control techniques (GNC) [1-3]. Although, many different combinations of electronic systems are used (FPGAs, DSPs, cameras, IMUs, GPSs, radars, spectrometers, etc), it is attractive to base the GNC algorithms in few elements, in order to increase the global reliability of the aerial vehicle. This work addresses the guidance of an autonomous glider with a technique that uses a camera as the main sensor and algorithms based on the epipolar geometry.

In general, the use of computer vision data in robot motion control is known as *visual servo control*, and the use of visual-feedback control loop to increase the accuracy of the robot motion system is known as *visual servoing* [4]. The epipolar geometry has been widely studied and used for wheeled-robot navigation, but its use for the guidance of aerial vehicles it is still an open research area. In [5], Chaumette and Hutchinson describe the use of epipolar geometry to estimate 3-D parameters of the camera pose, given two views of the same scene. In their approach, the

fundamental matrix is computed using a set of corresponding points between two images. The main drawback of this technique occurs when the current and desired images coincide, since the epipolar geometry becomes degenerate and other formulations, such as the homography, are preferred for the visual control. Hybrid and switching techniques, that join the epipolar geometry and the homography, are then proposed as a solution for the visual servo control of a robot.

In [6], Rives proposes an image-based visual servoing navigation method based on the motion of interest points over the image to reach their respective epipolar lines using two steps: robot rotations, and robot translation along the epipolar line. Mariottini et al. propose in [7,8] an image-based visual servoing algorithm for nonholonomic mobile robots, using also two steps: first the control uses input-output linearization to regulate the current epipole and to align the robot with the line along the optical axis of the desired camera, and then, the control advances the robot to the desired position. No knowledge of the 3-D scene is required and asymptotic convergence is proved.

López-Nicolás et al. show in [9] an epipolar visual servoing technique that includes into the design of the control law the nonholonomic constraints of a mobile robot. Two views are used to facilitate the teach-by-showing visual servo approach and no specific knowledge of the scene is required. The epipolar coordinates are used as inputs for the nonlinear system, and input-output linearization is used to design the control law. In [10,11], López-Nicolás et al. propose a switching control for mobile robots based on the epipolar geometry and homography. The switched controllers are designed using exact input-output linearization. The goal of this switching control is to produce a smooth robot motion activating the alternative control when an ill-conditioned situation is detected. Discontinuities due to the switching are avoided feeding back the velocities of one control to the other one.

Many advances in visual servo control applied to GNC of aerial vehicles have been also developed recently. Most of them use state estimation based on visual data and Kalman filters. For example, in [12], Gurfil and Rotstein use an *implicit* extended Kalman filter (IEKF) to estimate the states of an aircraft. The filter includes noisy measurements and the aircraft velocity vector calculated in camera axes by means of the so-called *implicit constraint*. The use of the IEKF reduces the noise due to the vehicle motion. In recent works [13,14], Indelman et al. propose a new vision-

based navigation aiding technique for navigation. This technique uses the constraints derived from general three-view geometry, and inertial navigation information to improve the estimation of the position of the aerial vehicle. The fusion of the information is done by means of an IEKF that also estimates the drift and bias errors of the inertial navigation system (INS). This technique is used to solve position estimation in GPS-denied environments and for cooperative navigation. Other contributions of this technique are the handling of loops (a vehicle revisits the same area) and the reduced computation load against other methods of localization. This technique keeps the estimated vector size as a constant and it relegates the scene reconstruction as a secondary task.

In [15], Webb et al. deal with the problem of state estimation for autonomous micro aerial vehicles (MAV). They use an IEKF plus epipolar geometry computed from feature points estimated with image processing. Under this configuration, it has been proved that the filter compensates significant modeling and initial condition errors. In [16], Koch et al. propose an extended Kalman filter (EKF) for sensor data fusion and for unmanned aerial vehicle (UAV) navigation. The filter uses vision data from ground features, tracked by the Lucas-Kanade Feature Tracker method, in order to compensate GPS failures. The position of ground features is determined as long as GPS data is available. When GPS fails, the position of new features is computed from the states that are estimated from the vision-based filter.

Johnson et al. [17] describe two vision-based methods to estimate the range of an aircraft relative to a target. A single camera provides measurements of the target in the image plane, and both, the velocity and the position of the aircraft relative to the target, are estimated by means of an EKF. In [18], Ma et al. propose a guidance law for a small UAV using a vision-based tracking of a target moving on the ground. Measurements of the target position in the image plane of a single camera are used in an adaptive estimator, which feeds back the guidance law in order to maintain the vehicle tracking the target at a given horizontal distance. The vehicle makes a circular orbit of a predefined radius keeping the target at the center of the orbit. In an early work [19], the same authors addressed the problem of tracking a ground vehicle, with unknown time-varying velocity, stabilizing the tracking horizontal distance to the target, to a constant value. A fast-estimation algorithm is used to estimate the time-varying target's velocity and an inverse-kinematic-based controller is used

to stabilize the horizontal range. Two controllers and a switching scheme are designed respectively for the case when visual measurements are available and the case when *out-of-frame* events occurs (target is out of the image plane). Stability analysis of both controllers is presented. A different approach is proposed in [20], where Martinez et al. use feature points estimated from the camera information, to maintain the consistency of image calculations with the image scale change, when the vehicle approaches to the target. They show simulations, seeking a laser marker temporarily occluded.

The use of homography for aircraft navigation and control has been reported by Kaiser et al. in [21], where a vision-based pose estimation method is proposed for an aerial vehicle to determine the current coordinates between successive images. The method is based on a series of geometric homography relationships, to create a series of *daisy-chained* pose estimates. This method ensures the mapping of landmarks in the world frame and can estimate the position of static features that leave the field of view (FoV) of the camera. The problem of degradation or instability of the visual servo control when the features leave the FoV has been previously addressed. For instance, in [22], homography relationships and image geometry are used to estimate the positions of feature points in the FoV of satellites. Also, in [23], Lee et al. present an adaptive image-based visual servoing control integrated with an adaptive sliding mode control for the operation of a small UAV (a quadrotor). The control objective is to keep the image features into the image plane, using the position and angular rate data from both a motion capture system and an inertial measurement unit (IMU).

In this paper, we present two guidance strategies for an autonomous glider, a class of aerial vehicles equipped with a single camera. These strategies are based on the epipolar coordinates that can be computed from two overlapping images using the geometry of two views. As it is noted by Indelman et al. in [14], the use of only two views gives information about the camera orientations, and the range between the camera centers cannot be computed directly. Additional information, such as inertial navigation, is necessary to improve the estimation of the aerial vehicle actual position. In our research, we use only two views, since the use of the camera orientation and the stabilization of the line of sight (LoS), will guide the glider to the desired position, and eventually intercept that position in a given future time.

In a previous work [24] we have proposed two strategies of guidance using the engagement rule between the camera centers, the proportional navigation concept, and input-output linearization. In this paper, we present a new state space representation of a full closed-loop system, including external disturbance input, establishing the basis for stability analysis. In the full closed-loop system, the vehicle's angular acceleration is considered as an external input and conditions for asymptotic stability and ultimate boundedness are established for both strategies. The estimation of the range between the vehicle and the target is avoided and only vision-based data is required to guide the vehicle to a desired position. In addition, we include a simple attitude control, achieved by the stabilization of two angles: the lead angle and the LoS angle. The analysis is constrained to motion on a vertical plane so the actuation (lateral acceleration) is perpendicular to the LoS in this plane. In addition, the camera is considered aero-stabilized, i.e., the orientation of its principal axis is parallel to the glider's velocity vector.

The paper is organized as follows: Sec. II describes the concepts of the epipolar geometry, the engagement system, and the design of the epipolar guidance strategies. Sec. III presents the stability analysis for both guidance methods. In Sec. IV simulation experiments are shown and, finally, conclusions are presented in Sec. V.

II.   Design of the Guidance Strategies

In this section, we present a brief overview of the main concepts and properties of the epipolar geometry, the engagement system, and the development of the guidance strategies.

A.   Epipolar Geometry

The epipolar geometry is the intrinsic geometric relationship between two views of a given scene (Fig. 1). It is totally defined by the relative poses and the intrinsic parameters of both cameras, i.e., by the fundamental matrix $\mathbf{F} \in \mathbb{R}^{3\times3}$ [25]. $\mathbf{F}$ describes the mapping of any point from one view to its matching point in the other view. As in [10] and [11], the first view is generated by the camera on-board the vehicle, and is called the *current* view. The other is the *target* view, and can be obtained and loaded into memory offline. The scenes of these two views must overlap.

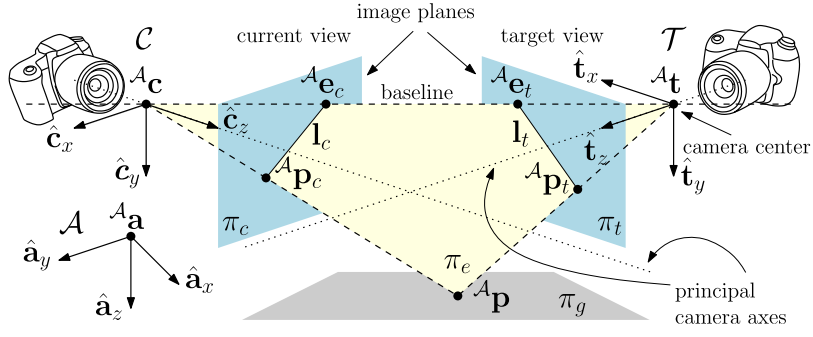The following coordinate systems are defined: the inertial NED (North-East-Down) coordinate

7

Fig. 1 3-D Epipolar Geometry.

system $\mathcal{A} : \{\hat{\mathbf{a}}_x, \hat{\mathbf{a}}_y, \hat{\mathbf{a}}_z\}$, with origin at $^{\mathcal{A}}\mathbf{a} \in \mathbb{R}^3$; the current camera-fixed coordinate system $\mathcal{C} : \{\hat{\mathbf{c}}_x, \hat{\mathbf{c}}_y, \hat{\mathbf{c}}_z\}$, with origin at $^{\mathcal{A}}\mathbf{c} \in \mathbb{R}^3$ (current camera center); and the target camera-fixed coordinate system $\mathcal{T} : \{\hat{\mathbf{t}}_x, \hat{\mathbf{t}}_y, \hat{\mathbf{t}}_z\}$, with origin at $^{\mathcal{A}}\mathbf{t} \in \mathbb{R}^3$ (target camera center). $\mathcal{C}$ and $\mathcal{T}$ are aligned with their correspondent image planes: π_c for the current view and π_t for the target view.

The *baseline* is the straight line passing through the camera centers. The *epipoles* are the projections of each camera center onto the image plane of the other camera, so the current epipole $^{\mathcal{A}}\mathbf{e}_c \in \mathbb{R}^3$, and the target epipole $^{\mathcal{A}}\mathbf{e}_t \in \mathbb{R}^3$, are the intersections between the baseline and the image planes π_c and π_t, respectively. The π_e-plane that contains the baseline is called the *epipolar plane*, and the intersections between π_e and the image planes are respectively the *epipolar lines* $\mathbf{l}_c$ and $\mathbf{l}_t$. $^{\mathcal{C}}\mathbf{p}_c \in \mathbb{R}^3$ and $^{\mathcal{T}}\mathbf{p}_t \in \mathbb{R}^3$ are the projections of the point $^{\mathcal{A}}\mathbf{p} \in \mathbb{R}^3$ onto the respective image planes π_c and π_t. Homogeneous coordinates are preferred over Cartesian coordinates to represent geometric entities such as points, lines and planes [25].

The matrix $\mathbf{F}$ can be computed mapping $^{\mathcal{C}}\mathbf{p}_c \mapsto {}^{\mathcal{T}}\mathbf{p}_t$ and then $^{\mathcal{T}}\mathbf{p}_t \mapsto \mathbf{l}_t$. Therefore, the relationship between $^{\mathcal{C}}\mathbf{p}_c$ and $\mathbf{l}_t$ can be written as [25]

$$\mathbf{l}_t = [^{\mathcal{T}}\mathbf{e}_t]_\times \mathbf{H}_g \left(^{\mathcal{C}}\mathbf{p}_c \right)$$
$$= \mathbf{F} \left(^{\mathcal{C}}\mathbf{p}_c \right) \quad , \tag{1}$$

where $\mathbf{F} = [^{\mathcal{T}}\mathbf{e}_t]_\times \mathbf{H}_g$, $[^{\mathcal{T}}\mathbf{e}_t]_\times \in \mathbb{R}^{3 \times 3}$ is a skew-symmetric matrix based on $^{\mathcal{T}}\mathbf{e}_t = {}^{\mathcal{T}}[e_{t,x}, e_{t,y}, e_{t,z}]^T$ (homogeneous representation of the target epipole), and $\mathbf{H}_g \in \mathbb{R}^3$ is a homography based on the ground plane π_g that contains the point $^{\mathcal{A}}\mathbf{p}$. In addition, since the projection $^{\mathcal{T}}\mathbf{p}_t$ belongs to its respective epipolar line $\mathbf{l}_t$, or $\left(^{\mathcal{T}}\mathbf{p}_t \right)^T \mathbf{l}_t = 0$, the following property of $\mathbf{F}$

8

and its relationships with the epipoles can be derived:

$$\left(^{\mathcal{T}}\mathbf{p}_t\right)^T \mathbf{F}\left(^{\mathcal{C}}\mathbf{p}_c\right) = 0 \tag{2a}$$

$$\mathbf{F}\left(^{\mathcal{C}}\mathbf{e}_c\right) = \mathbf{0} \tag{2b}$$

$$\mathbf{F}^T\left(^{\mathcal{T}}\mathbf{e}_t\right) = \mathbf{0} \quad . \tag{2c}$$

Hence, the following remark about the use of feature correspondences to compute the epipolar points can be established.

Remark 1. If a set of a minimum size N of feature correspondences (pairs in homogeneous coordinates), $\mathcal{F}_k = \left\{\left(^{\mathcal{C}}\hat{\mathbf{p}}_{c,i},^{\mathcal{T}}\hat{\mathbf{p}}_{t,i}\right)_k \mid \left(^{\mathcal{T}}\hat{\mathbf{p}}_{t,i}\right)^T \hat{\mathbf{F}}_k \left(^{\mathcal{C}}\hat{\mathbf{p}}_{c,i}\right) = 0 \; ; \; i = 1,\ldots,N\right\}$, is retrieved, at a time t_k, from the current view and the target view, then the fundamental matrix $\hat{\mathbf{F}}_k$ can be estimated uniquely (only for the current pair of views) and up to scale for the time t_k. Consequently, an estimation of the epipoles, $\left(^{\mathcal{C}}\hat{\mathbf{e}}_{c,k},^{\mathcal{T}}\hat{\mathbf{e}}_{t,k}\right)$, can be performed so that $\hat{\mathbf{F}}_k\left(^{\mathcal{C}}\hat{\mathbf{e}}_{c,k}\right) = \mathbf{0}$ and $\hat{\mathbf{F}}_k^T\left(^{\mathcal{T}}\hat{\mathbf{e}}_{t,k}\right) = \mathbf{0}$ (for this purpose, there are many proposed algorithms [22]).

For the case of motion in a vertical plane, some simplifications can be introduced (Fig. 2). Camera's rotational motion are described with simple angular velocities: $\dot{\gamma}_c\hat{\mathbf{c}}_x = \dot{\gamma}_c\hat{\mathbf{a}}_y$ for the current camera, and $\dot{\gamma}_t\hat{\mathbf{t}}_x = \dot{\gamma}_t\hat{\mathbf{a}}_y$ for the target camera. γ_c and γ_t are the respective instantaneous orientations, or *flight-path* angles, measured with respect to a horizon parallel to the $\hat{\mathbf{a}}_x$-axis.

The instantaneous separation between the camera centers will define the magnitude of the *range* vector

$$^{\mathcal{A}}\mathbf{r}_{c,t} = {}^{\mathcal{A}}\mathbf{r}_{a,t} - {}^{\mathcal{A}}\mathbf{r}_{a,c} \quad , \tag{3}$$

where $^{\mathcal{A}}\mathbf{r}_{a,t}$ is the position vector of the target camera center, $^{\mathcal{A}}\mathbf{t}$, and $^{\mathcal{A}}\mathbf{r}_{a,c}$ is the position vector of the current camera center, $^{\mathcal{A}}\mathbf{c}$. In addition, $^{\mathcal{A}}\mathbf{r}_{c,t}$ matches the baseline, which is the same *Line of Sight* (LoS) named $\mathcal{CT}$-LoS in Fig. 2. The camera velocity angles, μ_c and μ_t, measured with respect to the $\mathcal{CT}$-LoS, are the *lead* and the *aspect* angles [26]. The orientation of the $\mathcal{CT}$-LoS with respect to the $\hat{\mathbf{a}}_x$-axis is commonly denoted as λ. Then, the lead and aspect angles can be written, in terms of λ, as
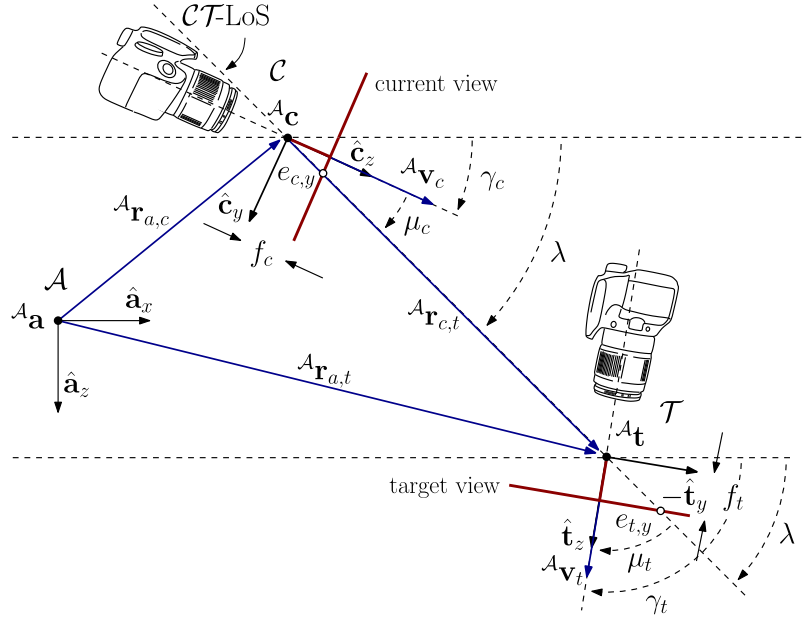
Fig. 2 2-D Epipolar Geometry.

$$\mu_c = (\lambda - \gamma_c) \tag{4a}$$

$$\mu_t = (\gamma_t - \lambda) \quad . \tag{4b}$$

If the current and target epipoles are represented in Cartesian coordinates, relative to $\mathcal{C}$ and $\mathcal{T}$, as $^{\mathcal{C}}\mathbf{e}_c = [e_{c,x}, e_{c,y}, e_{c,z}]^T$ and $^{\mathcal{T}}\mathbf{e}_t = [e_{t,x}, e_{t,y}, e_{t,z}]^T$, the epipolar coordinates $e_{c,y}$ and $e_{t,y}$ result as

$$e_{c,y} = f_c \tan\left(\mu_c\right) \tag{5a}$$

$$e_{t,y} = -f_t \tan\left(\mu_t\right) \quad , \tag{5b}$$

where f_c and f_t are the focal lengths of the current and target cameras. If we substitute Eq. (4a) and Eq. (4b) it yields

$$e_{c,y} = f_c \tan\left(\lambda - \gamma_c\right) \tag{6a}$$

$$e_{t,y} = -f_t \tan\left(\gamma_t - \lambda\right) \quad . \tag{6b}$$

10

The last two equations show the relationship between the epipolar coordinates, $e_{c,y}$ and $e_{t,y}$, and the $\mathcal{CT}$-LoS angle, λ, enabling the definition of guidance based on epipolar coordinates.

B.   Engagement System

We define the $\mathcal{CT}$-system as the state space representation of the engagement of the current and target cameras (Fig. 3). The $\mathcal{CT}$-LoS angle, λ, is equal to

Fig. 3 Engagement system.

$$\lambda = \arctan \frac{z}{x} \quad , \tag{7}$$

where x and z are the range components along the $\hat{\mathbf{a}}_x$-axis and the $\hat{\mathbf{a}}_z$-axis. The $\mathcal{CT}$-LoS rate of change, $\dot{\lambda}$, can be computed by differentiation of Eq. (7) with respect to t

$$\dot{\lambda} = \frac{\dot{z}x - z\dot{x}}{r_{c,t}^2} \quad , \tag{8}$$

where $r_{c,t} = \sqrt{x^2 + z^2}$ is the magnitude of the range $^{\mathcal{A}}\mathbf{r}_{c,t}$. Differentiating Eq. (8), with respect to t, it follows that

$$\ddot{\lambda} = \frac{1}{r_{c,t}^2}\left(\ddot{z}x - z\ddot{x}\right) - 2\frac{\dot{r}_{c,t}}{r_{c,t}}\dot{\lambda} \quad . \tag{9}$$

In addition, if the target camera is static, ${}^{\mathcal{A}}\dot{\mathbf{r}}_{c,t} = -{}^{\mathcal{A}}\dot{\mathbf{r}}_{a,c}$, which is the negative of the *closing velocity*. If the aerial vehicle can generate a lateral acceleration ${}^{\mathcal{A}}\mathbf{n} = {}^{\mathcal{A}}[n_x, 0, n_z]^T$, perpendicular to the $\mathcal{CT}$-LoS, then, the components of ${}^{\mathcal{A}}\ddot{\mathbf{r}}_{c,t}$, $\ddot{x}$ and $\ddot{z}$, and the lateral acceleration components, n_x and n_z, will be related by the following equations

$$\ddot{x} = -n_x = -n\sin\lambda \tag{10a}$$

$$\ddot{z} = n_z = n\cos\lambda \quad, \tag{10b}$$

where n is the magnitude of ${}^{\mathcal{A}}\mathbf{n}$. Also, from Fig. 3, it can be seen that

$$\frac{x}{r_{c,t}} = \cos\lambda \tag{11a}$$

$$\frac{z}{r_{c,t}} = \sin\lambda \quad. \tag{11b}$$

Then, using Eq. (10a)-Eq. (11b), in Eq. (9), it results that

$$\ddot{\lambda} = -2\frac{\dot{r}_{c,t}}{r_{c,t}}\dot{\lambda} + \frac{1}{r_{c,t}}n \quad. \tag{12}$$

Finally, the $\mathcal{CT}$-system state space representation is

$$\dot{\eta} = \mathbf{A}\eta + \mathbf{B}u \quad, \tag{13}$$

where $\eta = [\eta_1, \eta_2]^T = [\lambda, \dot{\lambda}]^T$ is the state vector, $u = n$ is the control input, and

$$\mathbf{A} = \begin{bmatrix} 0 & 1 \\ 0 & -2\dfrac{\dot{r}_{c,t}}{r_{c,t}} \end{bmatrix} \quad \mathbf{B} = \begin{bmatrix} 0 \\ \dfrac{1}{r_{c,t}} \end{bmatrix} \quad, \tag{14}$$

are the state matrix and input vector, respectively. $\mathbf{A}$ and $\mathbf{B}$ depend on the range magnitude and its rate of change, which in turn implicitly depend on t. The system in Eq. (13) is continuous, linear, and time-varying. It has an equilibrium subspace equal to the η_1-axis, and its stability can

be directly computed from $\mathbf{A}$. Because of the eigenvalues of $\mathbf{A}$ are $\Lambda_{1,2} = \{0, -2\dot{r}_{c,t}/r_{c,t}\}$, only marginal stability [27] about η_2 is concluded.

Traditionally, the guidance of an aerial vehicle is performed by a porportional navigation (PN) law [28], which measures the states and the range by means of inertial sensors, seekers, and/or external agents that guide the vehicle to a desired target position [29]. In this work, the current camera is the main sensor that will be used to feed back the guidance methods that we propose in the following section.

C. Epipole-Based Guidance

Two strategies are proposed: the current epipole-based guidance (CEBG) and the target epipole-based guidance (TEBG). Both methods are based on the assumption that stabilization of the epipolar coordinates could guide an aerial vehicle to the position of a fixed target camera. The CEBG makes the output of the $\mathcal{CT}$-system equal to the current epipolar coordinate, $e_{c,y}$, and the TEBG makes the output equal to the target epipolar coordinate, $e_{t,y}$. Using the subscript i to denote c, for the current camera, or t, for the target camera, both outputs can be written as

$$y_i = e_{i,y} \quad . \tag{15}$$

Considering Eq. (6a) and Eq. (6b), the above formulation leads to a nonlinear system with respect to the η_1-state. Then, a mapping from these nonlinear outputs to linear outputs can be achieved by means of the input-output linearization method [30]. In this context, and since the input u of the $\mathcal{CT}$-system becomes explicit at the second derivative of each output, the *relative degree* for each output is the same and equal to 2. Then, the following transformation

$$\xi_{i,1} = y_i = e_{i,y} \tag{16a}$$

$$\xi_{i,2} = \dot{\xi}_{i,1} = \dot{y}_i = \dot{e}_{i,y} \tag{16b}$$

$$\dot{\xi}_{i,2} = \ddot{\xi}_{i,1} = \ddot{y}_i = \ddot{e}_{i,y} = v_i \quad , \tag{16c}$$

maps the nonlinear output y_i into the linearized output

13

$$\dot{\xi}_i = \mathbf{A}_i \xi_i + \mathbf{B}_i v_i \quad, \tag{17}$$

where $\xi_i = [\xi_{i,1}, \xi_{i,2}]^T$ is the linearized output state and

$$\mathbf{A}_i = \begin{bmatrix} 0 & 1 \\ 0 & 0 \end{bmatrix} \quad \mathbf{B}_i = \begin{bmatrix} 0 \\ 1 \end{bmatrix} \quad, \tag{18}$$

are the respective linearized output state matrix and the linearized output control vector. $v_i \in \mathbb{R}$ is the control input that eliminates the nonlinearities of its respective output y_i, if and only if, it is related to the $\mathcal{CT}$-system input, u, given the following conditions: For the output y_c, in $\mathbb{R}^2$ and for all η, with

$$
\begin{aligned}
u_c = {} & \frac{r_{c,t}}{f_c \sec^2 (\eta_1 - \gamma_c)} v_c + 2\dot{r}_{c,t}\eta_2 + r_{c,t}\ddot{\gamma}_c \\
& - 2r_{c,t}(\eta_2 - \dot{\gamma}_c)^2 \tan(\eta_1 - \gamma_c) \quad .
\end{aligned} \tag{19}
$$

And, for the output y_t, in $\mathbb{R}^2$ and for all η, with

$$
\begin{aligned}
u_t = {} & \frac{r_{c,t}}{f_t \sec^2 (\gamma_t - \eta_1)} v_t + 2\dot{r}_{c,t}\eta_2 \\
& + 2r_{c,t}\eta_2^2 \tan(\gamma_t - \eta_1) \quad .
\end{aligned} \tag{20}
$$

After this linearization, each guidance method is designed to stabilize the corresponding linear output, $\xi_{i,1}$, to an epipolar reference $\xi_{i,1,r} = e_{i,y,r} \in \mathbb{R}$. Using an integral action we ensure the tracking of the epipolar coordinate and the rejection of input disturbances and plant parameter variations [27][30]. It is assumed that $\xi_{i,1}$ is measured as $y_{m,i} = \mathbf{C}_i \xi_i$, with $\mathbf{C}_i = [1, 0]$. Therefore, the tracking error σ_i, for each method, results as

$$
\begin{aligned}
\dot{\sigma}_i &= y_{m,i} - \xi_{i,1,r} \\
&= \mathbf{C}_i \xi_i - \xi_{i,1,r} \quad .
\end{aligned} \tag{21}
$$

Thus, if the state σ_i is augmented to the linearized output in Eq. (17), and state feedback control

14

$$v_i = -\mathbf{K}_i[\xi_i^T, \sigma_i]^T + \omega_i \quad , \tag{22}$$

with $\mathbf{K}_i = [k_{i,1}, k_{i,2}, k_{i,3}]$ ($\mathbf{K}_i^T \in \mathbb{R}^3$), is applied to the input of each linearized output ($\omega_i \in \mathbb{R}$ is an input disturbance that can represent linearization and measurement errors), then, the closed-loop augmented linearized output becomes

$$\dot{\mathbf{x}}_i = \mathbf{A}_{i,a}\mathbf{x}_i + \mathbf{B}_{i,a}\omega_i + \bar{\mathbf{B}}_{i,a}\xi_{i,1,r} \tag{23a}$$

$$y_{m,i} = \begin{bmatrix} \mathbf{C}_i & 0 \end{bmatrix} \mathbf{x}_i \quad , \tag{23b}$$

where $\mathbf{x}_i = [\xi_i^T, \sigma_i]^T$ is the closed-loop augmented linearized output state, and

$$\mathbf{A}_{i,a} = \begin{bmatrix} \mathbf{A}_i - \mathbf{B}_i[k_{i,1}, k_{i,2}] & -\mathbf{B}_i k_{i,3} \\ \mathbf{C}_i & 0 \end{bmatrix} \quad \mathbf{B}_{i,a} = \begin{bmatrix} \mathbf{B}_i \\ 0 \end{bmatrix} \quad \bar{\mathbf{B}}_{i,a} = \begin{bmatrix} \mathbf{0}_{2\times 1} \\ -1 \end{bmatrix} \quad , \tag{24}$$

are respectively the augmented state matrix and the augmented input vectors of the closed-loop augmented linearized output.

It can be easily verified that the pair $(\mathbf{A}_i, \mathbf{B}_i)$ is controllable and that the transfer function $\mathbf{C}_i(s\mathbf{I}_{2\times 2} - \mathbf{A}_i)^{-1}\mathbf{B}_i$ has no zero in $s = 0$. Therefore, all the eigenvalues of $\mathbf{A}_{i,a}$ can be assigned arbitrarily by means of the gain vector $\mathbf{K}_i$ [27]. We choose $\mathbf{K}_i$ such that $\mathbf{A}_{i,a}$ is Hurwitz, since this guarantees the epipolar coordinate follows the reference.

Finally, we define a full closed-loop system, as the composition of the closed-loop augmented linearized output, Eq. (23a), plus the closed-loop $\mathcal{CT}$-system, Eq. (13). It is observed that both epipolar guidance strategies share the same equation form for the closed-loop augmented linearized output, whereas the equation form of the closed-loop $\mathcal{CT}$-system only changes in one term that depends on the relationship between the inputs u_i and v_i (Eq. (19) for the CEBG, and Eq. (20) for the TEBG). The full closed-loop system can be written as

$$\dot{\chi}_i = f(\chi_i) + W_i \quad , \tag{25}$$

where $\chi_i = [\eta^T, \mathbf{x}_i^T]^T$ is the full closed-loop system state,

$$f(\chi_i) = \begin{bmatrix} \eta_2 \\ -\dfrac{f_i}{\xi_{i,1}^2 + f_i^2}\left(k_{i,1}\xi_{i,1} + k_{i,2}\xi_{i,2} + k_{i,3}\sigma_i + 2\dfrac{\xi_{i,1}\xi_{i,2}^2}{\xi_{i,1}^2 + f_i^2}\right) \\ \mathbf{A}_{i,a}\mathbf{x}_i + \bar{\mathbf{B}}_{i,a}\xi_{i,1,r} \end{bmatrix} \quad , \tag{26}$$

and

$$W_i = \begin{bmatrix} 0 \\ \dfrac{f_i\omega_i}{\xi_{i,1}^2 + f_i^2} + \kappa_i \\ \mathbf{B}_{i,a}\omega_i \end{bmatrix} \quad . \tag{27}$$

κ_i has been defined to be $\ddot{\gamma}_i$. When $i = c$, $\kappa_c = \ddot{\gamma}_c$, and when $i = t$, $\kappa_t = \ddot{\gamma}_t = 0$. Stability of the full closed-loop system will be analyzed in the next section.

III. Stability Analysis

The nonlinear system in Eq. (25) can be thought as a system that is composed of a nominal system, $f(\chi_i)$, and an input perturbation, W_i. For the CEBG, we can view $\ddot{\gamma}$ as an external perturbation that is related to the airframe stability of the vehicle that carries the current camera; whereas, for the TEBG, since the target camera is static ($\dot{\gamma}_t = \ddot{\gamma}_t = 0$), we can say that the guidance is free of this external perturbation. For the stability analysis, two cases for both strategies are considered: the case of the full closed-loop system with $\omega_i = 0$, and the case of the full closed-loop system with $\omega_i \neq 0$.

A. Stability of the Full Closed-Loop System with $\omega_i = 0$

If $\omega_i = 0$, we observe, from Eq. (25) - Eq. (27), that the full closed-loop system $\dot{\chi}_i = f(\chi_i) + \ddot{\gamma}_i$, and its equilibrium depends on the perturbation input γ_i. The following corollary, based on Theorem 4.5 in [30], states the stability properties of this system.

Corollary 1. Let $\omega_i = 0$, the matrix $\mathbf{A}_{i,a}$ to be Hurtwitz, and the angular velocity $\dot{\gamma}_i$ to be a vanishing perturbation. Then, and for all $t > t_d$ ($t_d > 0$): (i) The full closed-loop system in Eq. (25) has the equilibrium subspace

$$\chi_{i,ss} = \left[\gamma_i + m_i, \ 0, \ \xi_{i,1,r}, \ 0, \ -\frac{k_{i,1}}{k_{i,3}} \xi_{i,1,r} \right]^T \quad , \tag{28}$$

where $m_i = \arctan\left(\xi_{i,1,r}/f_i\right)$. (ii) The origin, $\chi_{i,ss} = \mathbf{0}$, is asymptotically stable.

Proof. See Appendix A. $\qquad\square$

The stability of the TEBG is completely defined by the above corollary because the path angle γ_t is always assumed as a constant value ($\dot{\gamma}_t = \ddot{\gamma}_t = 0$ for all $t > 0$). In contrast, for the CEBG, since the value of the perturbation $\dot{\gamma}_c$ depends on the vehicle's dynamics, the stability of the full closed-loop system will depend on the airframe's equilibrium, and specifically, if γ_c is an equilibrium of the airframe. If γ_c is a constant for all $t > t_d$, then the stability of the CEBG is completely defined by this Corollary.

B. Stability of the Full Closed-Loop System with $\omega_i \neq 0$

When $\omega_i \neq 0$, the full closed-loop system in Eq. (25) results as $\dot{\chi}_i = f(\chi_i) + \ddot{\gamma}_i$ but perturbed by an additional term that depends on ω_i. Since ω_i has direct influence on both the η_2-state and the $\mathbf{x}_i$-state, then, an assumption of the nature of ω_i and γ_i needs to be established to conclude about the stability of the full closed-loop system. The following corollary, based on Lemma 9.3 and Lemma 13.3 in [30], defines the stability of the perturbed full closed-loop system.

Corollary 2. Let the matrix $\mathbf{A}_{i,a}$ to be Hurtwitz, $\mathbf{P}_i = \mathbf{P}_i^T$ to be a positive definite matrix that is the unique solution of the Lyapunov equation $\mathbf{P}_i \mathbf{A}_{i,a} + \mathbf{A}_{i,a}^T \mathbf{P}_i = -\mathbf{I}$, and k a nonnegative constant such that $k \leq 1/(2\|\mathbf{P}_i \mathbf{B}_{i,a}\|)$.

(i) If both ω_i and $\dot{\gamma}_i$ are vanishing perturbations, then, and for all $t > t_d$ ($t_d > 0$), the full closed-loop system, in Eq. (25), has the equilibrium subspace that is shown in Eq. (28), and the origin it has, $\chi_{i,ss} = \mathbf{0}$, is asymptotically stable.

(ii) If $\dot{\gamma}_i$ is a vanishing perturbation, and ω_i satisfies

$$\|\omega_i\| \leq k w_4(w_1) \quad , \tag{29}$$

for all $t \geq t_0 + T_1$, where $t_0 \geq t_d$ $(t_d > 0)$, and w_4 is a class $\mathcal{K}$ function that depends on the parameter w_1, then, the trajectories of the full closed-loop system, in Eq. (25), and for some finite time T_1, are ultimately bounded by

$$\|\chi_i\| \leq w_4(w_1) \quad , \quad \forall \quad t \geq t_0 + T_1 \quad . \tag{30}$$

(iii) If $\dot{\gamma}_i$ is not a vanishing perturbation, and

$$\left\| \frac{\omega_i}{f_i} + \ddot{\gamma}_i \right\| \leq k w_7(w_5) \quad , \tag{31}$$

for all $t \geq t_0 + T_2$, where $t_0 \geq t_d$ $(t_d > 0)$, and w_7 is a class $\mathcal{K}$ function that depends on the parameter w_5, then, the trajectories of the full closed-loop system, in Eq. (25), and for some finite time T_2, are ultimately bounded by

$$\|\chi_i\| \leq w_6(w_5) \quad , \quad \forall \quad t \geq t_0 + T_2 \quad . \tag{32}$$

Proof. See Appendix B. $\qquad\qquad\square$

It is noted from the above Corollary that: if condition in Eq. (29), or Eq. (31), are satisfied, and even though ω_i and/or $\dot{\gamma}_i$ could not be vanishing perturbations, then, the subsystem $\dot{\mathbf{x}}_i$ (in Eq. (23a)) still has an equilibrium that is exponentially stable. However, only ultimately boundedness is guaranteed for the full closed-loop system under the conditions that have been established.

IV. Simulation Experiments

To show the application of each guidance strategy, we use an autonomous glider, described in the following subsection, in a series of simulations with a set of initial conditions. A classical three-loop autopilot guarantees that the acceleration requirements are reached, without overcome the airframe's aerodynamic capabilities. We have assumed that both cameras have the same parameters: $f_i = 1$ mm (focal length), image plane size equal to 240×240 pixels/mm (height $\times$ width), skew

parameter zero, principal point offset at $(240, 320)$ pixels (height, width), and spatial resolution of 480×640 pixels (height $\times$ width).

A.   Aerial Vehicle Model

We use a glider provided with a horizontal control surface (wing) and a stabilizing fixed surface (tail). The control action is performed by the wing deflection angle δ [31]. Fig. 4 shows the wing-body-tail configuration. In this figure, $\mathcal{B} : \{\hat{\mathbf{b}}_x, \hat{\mathbf{b}}_y, \hat{\mathbf{b}}_z\}$ is the vehicle-fixed coordinate frame, which is aligned with the vehicle's principal axes, and is located at $^{\mathcal{A}}\mathbf{b} \in \mathbb{R}^3$ (the vehicle's center of gravity, CG).
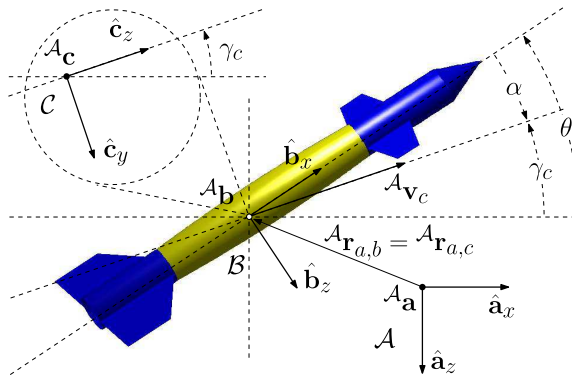
Fig. 4 Aerial vehicle in the $\hat{\mathbf{a}}_x \hat{\mathbf{a}}_z$-plane.

For simplicity, the current camera center has been translated to CG, and it is assumed it always has an orientation parallel to the vehicle's velocity vector, $^{\mathcal{A}}\mathbf{v}_c$. Equations of motion of the vehicle can be found in [29]. Here, the following state space representation, in the $\hat{\mathbf{a}}_x \hat{\mathbf{a}}_z$-plane, is retrieved:

$$
\begin{aligned}
\dot{x}_1 &= x_3 \\
\dot{x}_2 &= x_4 \\
\dot{x}_3 &= -x_6 x_4 - g \sin x_5 - \frac{C_A q S_{ref}}{m} \\
\dot{x}_4 &= -x_6 x_3 - g \cos x_5 - \frac{C_N q S_{ref}}{m} \\
\dot{x}_5 &= x_6 \\
\dot{x}_6 &= \frac{q S_{ref} l_{ref} C_m}{I_{yy}} \quad ,
\end{aligned}
\tag{33}
$$

where x_1 is the longitudinal translation, x_2 is the vertical translation, x_3 is the longitudinal velocity, x_4 is the vertical velocity, $x_5 = \theta$ is the attitude angle, and $x_6 = \dot{\theta}$ is the angular velocity. m is the vehicle mass, g is the acceleration of gravity, I_{yy} is the principal moment of inertia around the $\hat{\mathbf{b}}_y$-axis, and, for small aerial vehicles, S_{ref} and l_{ref} are the respective maximum cross-sectional area and the mean diameter of the body's. The dynamic pressure is $q = (1/2)\rho V^2$, where V is the free-stream velocity and ρ is the air density. The angle of attack can be written as $\alpha = \arctan{(x_4/x_3)}$.

The aerodynamic coefficients C_A, C_N, and C_m, were estimated with Tornado Vortex-Lattice Method [32] and are described by the functions

$$
\begin{aligned}
C_A &= C_{A,\alpha}\alpha^2 + C_{A,\alpha,\delta}\alpha\delta + C_{A,\delta}\delta^2 \\
C_N &= C_{N,\alpha}\alpha + C_{N,\delta}\delta \\
C_m &= C_{m,\alpha}\alpha + C_{m,\delta}\delta \quad ,
\end{aligned}
\tag{34}
$$

where $C_{A,\alpha}$, $C_{A,\alpha,\delta}$, $C_{A,\delta}$, $C_{N,\alpha}$, $C_{N,\delta}$, $C_{m,\alpha}$, and $C_{m,\delta}$ are coefficients that depend on h (altitude) and M (Mach number). These coefficients are stored in look-up tables.

B. Autopilot

A classical autopilot provides the lateral acceleration required by the guidance methods. It translates the acceleration command, u_i (Eq. (19) for the CEBG and Eq. (20) for the TEBG), to wing deflection, δ. An autopilot's detailed description can be found in [33]. The autopilot's closed-loop gains: K_{DC}, K_A, ω_I, and K_R, depend on the scheduling variables, h and M, and are stored in look-up tables.

The parameters of the autopilot are set to: $\omega_{CR} = 10\,\text{rad/s}$ (cross-zero frequency), $\zeta = 1.0$ (total damping), and $\tau = 0.4\,\text{s}$ (total time constant). The autopilot was tested for combinations of several flight conditions. Fig. 5 shows the autopilot's response to the unit step reference, $n_{ref} = u_s(t-1)$ G of n (lateral acceleration), α (angle of attack), and δ (deflection angle).

When $M = 0.3$ and $M = 0.9$ the autopilot follows the reference u_{ref} (Fig. 5(a) and Fig. 5(b)). However, it is noticed that the settling time for low velocities is greater than for high velocities, and the response requires higher values for the angles α and δ (Fig. 5(c) and Fig. 5(e)). This means that

(a) n $(M = 0.3)$

(b) n $(M = 0.9)$

(c) α $(M = 0.3)$

(d) α $(M = 0.9)$

(e) δ $(M = 0.3)$
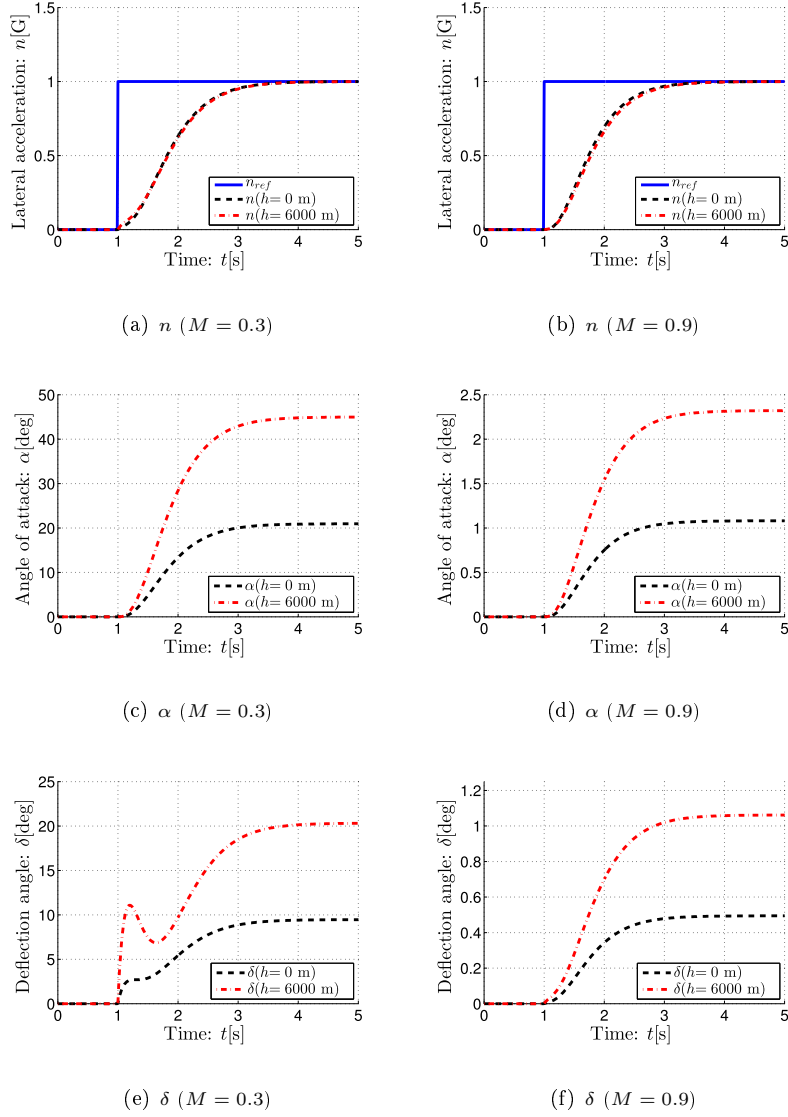
(f) δ $(M = 0.9)$

Fig. 5 Autopilot's response to $n_{ref} = u_s(t-1)$ G.

when there is not enough velocity, the vehicle aerodynamic capabilities can be exceeded and the system could become unstable. Also, the vehicle maneuverability for low altitude is greater than for high altitude.

C.   Experiments for the Current Epipole-Based Guidance

For these experiments, the following conditions are set: $h_0 = 4000$ m (vehicle initial altitude), ${}^{\mathcal{A}}\mathbf{a} = {}^{\mathcal{A}}[0, 0, h_0]$ m, ${}^{\mathcal{A}}\mathbf{t} = {}^{\mathcal{A}}[3000, 0, 3000]^T$ m, and $\gamma_t = 45$ deg. The gain $\mathbf{K}_c = [15, 5, 15]$ ensures the Hurtwitz condition for the matrix $\mathbf{A}_{c,a}$, which has the eigenvalues: $-1.7221 + i2.5838$, $-1.7221 - i2.5838$, and $-1.5558 + i0.0000$. Perturbation ω_c is assumed to be zero.

1.   Interception of a target camera

This experiment represents the interception of the target camera in three different initial conditions. The current epipolar coordinate reference is set to $\xi_{c,1,r} = e_{c,y,r} = 0$ pixels, and the initial conditions are associated with three current cameras: C_1, C_2, and C_3. The initial conditions for these cameras are: ${}^{\mathcal{A}}\mathbf{c}_{1,0} = {}^{\mathcal{A}}[0,0,h_0]^T$ m, ${}^{\mathcal{A}}\mathbf{c}_{2,0} = {}^{\mathcal{A}}[100,0,h_0]^T$ m, ${}^{\mathcal{A}}\mathbf{c}_{3,0} = {}^{\mathcal{A}}[200,0,h_0]^T$ m, ${}^{\mathcal{B}}\mathbf{v}_{c,1,0} = {}^{\mathcal{B}}\mathbf{v}_{c,2,0} = {}^{\mathcal{B}}\mathbf{v}_{c,3,0} = {}^{\mathcal{B}}[195,0,0]^T$ m/s, and $\gamma_{c,1,0} = \gamma_{c,2,0} = \gamma_{c,3,0} = 45$ deg. Fig. 6 shows the experiment results.

(a) Trajectory

(b) Lateral acceleration: n

(c) Current epipolar coordinate: $e_{c,y}$

(d) Target epipolar coordinate: $e_{t,y}$

(e) Angle of attack: α

(f) Wing deflection angle: δ
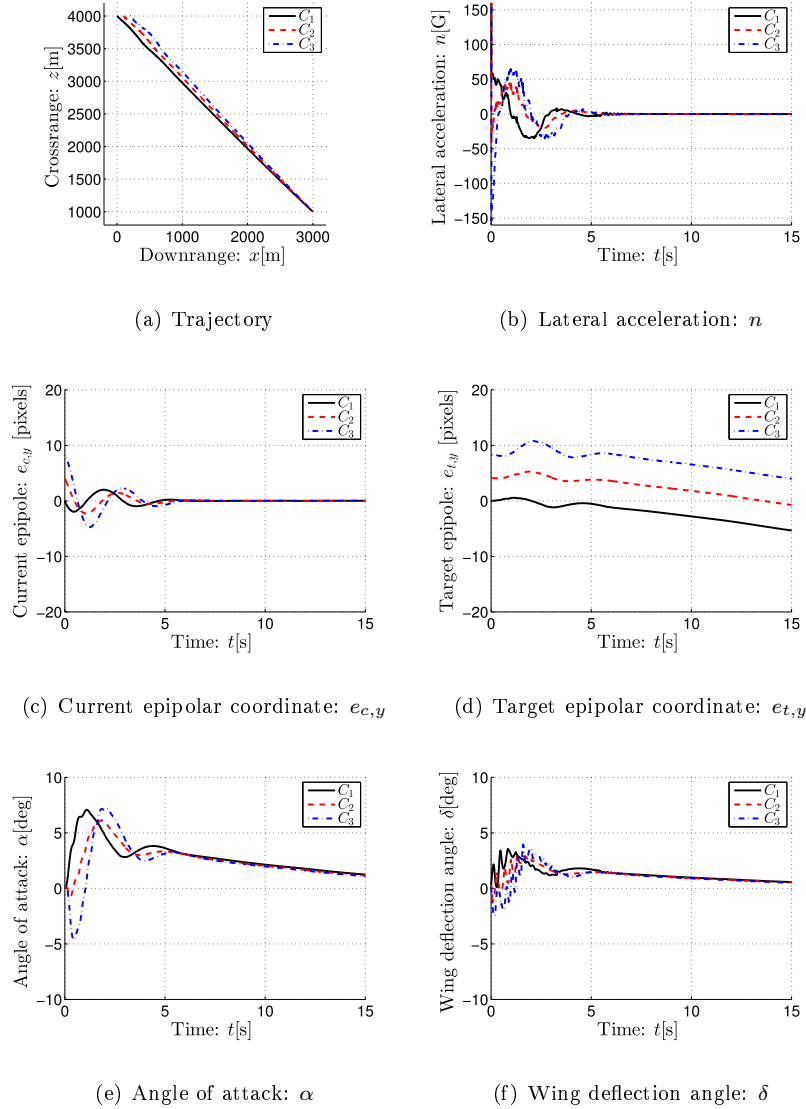
Fig. 6 Interception of a target camera. For all the initial conditions, $\xi_{c,1,r} = e_{c,y,r} = 0$.

Figure 6(a) shows the trajectories of each current camera approaching to the target camera

position. For each initial condition, and despite γ_c is not an equilibrium of the aerial vehicle, the guidance of the current cameras to the target camera position is ensured because $\xi_{c,1} = e_{c,y}$ is regulated by $\mathbf{K}_c$ (Fig. 6(c)). Fig. 6(d) shows the evolution of the target epipolar coordinate, $e_{t,y}$. Figure 6(b) shows the lateral acceleration, n, required for the vehicle. In the case C_3, a higher lateral acceleration is required. Fig. 6(e) and Fig. 6(f) show that α and δ does not exceed the aerodynamic and structural capabilities of the airframe and instability is avoided.

2. Lead angle control

This experiment shows the trajectory of the vehicle when the current epipolar reference is set to three different signals. Each reference is defined as $\xi_{c,1,r,j} = e_{c,y,r,j} = S_j[u_s(t) + u_s(t - 4) + u_s(t - 8)]$ pixels, with $j = 1, 2, 3$, $S_1 = 20$, $S_2 = -10$, and $S_3 = -40$. The current camera, C, has the initial conditions: $^\mathcal{A}\mathbf{c}_0 = {}^\mathcal{A}[0, 0, h_0]^T$ m, $^\mathcal{B}\mathbf{v}_{c,0} = {}^\mathcal{B}[195, 0, 0]^T$ m/s, and $\gamma_{c,0} = 45$ deg. Fig. 7 shows the experiment results.

Figure 7(a) shows the resulting trajectories. Since the references have a final nonzero value, and γ_c is not an equilibrium of the vehicle, then, the guidance of the current camera to the target camera position is not ensured. However, different trajectory shapes and control of the lead angle μ_c are achieved. Fig. 7(b) shows the tracking of the current epipolar references, and Fig. 7(c) shows the stabilization of the lead angle. For each case, the value of the lead angle is $\arctan(e_{c,y,r,j}/f_c)$ (Eq. (5a)). Fig. 7(d), Fig. 7(e), and Fig. 7(f), show respectively the values of n, α, and δ. In these figures, we can observe that when the current epipolar coordinate reaches a high absolute value, instability could not be avoided.

D. Experiments for the Target Epipole-Based Guidance

In these experiments, we choose the same values for $^\mathcal{A}\mathbf{a}$, $^\mathcal{A}\mathbf{t}$, γ_t, and $\mathbf{K}_t$, than for the CEBG experiments. Perturbation ω_t is assumed to be zero too.

(a) Trajectory

(b) Current epipolar coordinate: $e_{c,y}$

(c) Lead angle: μ_c

(d) Lateral acceleration: n

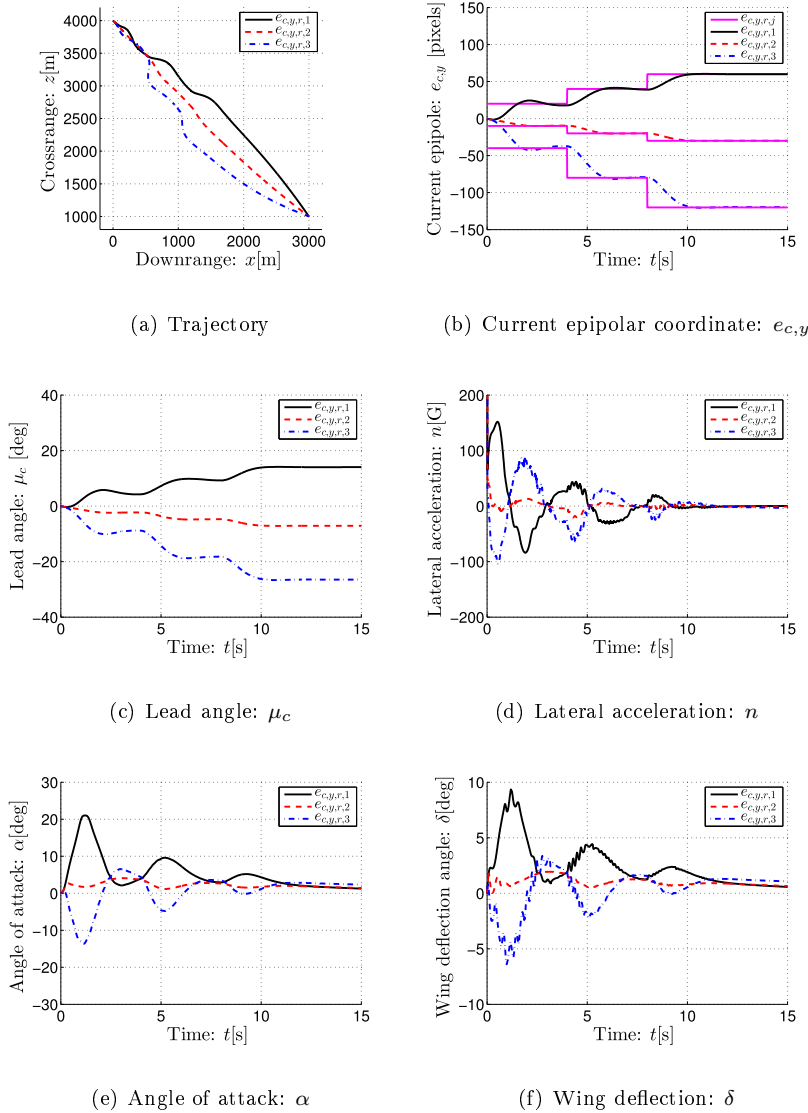(e) Angle of attack: α

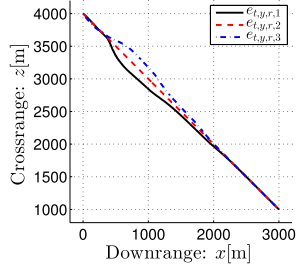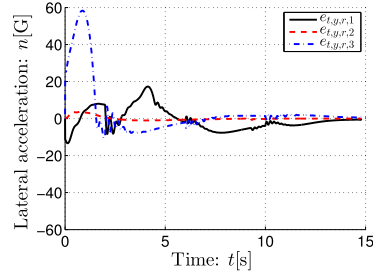(f) Wing deflection: δ

Fig. 7 Lead angle control.
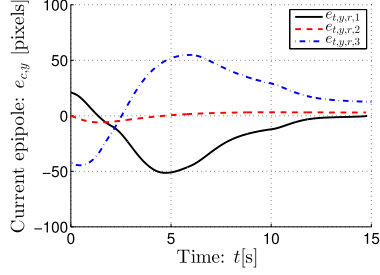
1. Interception of a target camera

This experiment shows the interception of the target camera in three different initial conditions, following three different target epipolar references. Each reference is defined as: $\xi_{t,1,r,1} = e_{t,y,r,1} = -[10u_s(t-2) - 5u_s(t-6) - 5u_s(t-10)]$ pixels, $\xi_{t,1,r,2} = e_{t,y,r,2} = 0$ pixels, and $\xi_{t,1,r,3} = e_{t,y,r,3} = 10u_s(t-2) - 5u_s(t-6) - 5u_s(t-10)$ pixels. The initial conditions are associated with three current cameras: C_1, C_2, and C_3, with the following values: ${}^{\mathcal{A}}\mathbf{c}_{1,0} = {}^{\mathcal{A}}\mathbf{c}_{2,0} = {}^{\mathcal{A}}\mathbf{c}_{3,0} = {}^{\mathcal{A}}[0,0,h_0]^T$ m, ${}^{\mathcal{B}}\mathbf{v}_{c,1,0} = {}^{\mathcal{B}}\mathbf{v}_{c,2,0} = {}^{\mathcal{B}}\mathbf{v}_{c,3,0} = {}^{\mathcal{B}}[240,0,0]$ m/s, $\gamma_{c,1,0} = 40$ deg, $\gamma_{c,2,0} = 45$ deg, and $\gamma_{c,3,0} = 55$ deg. Fig. 8 shows the experiment results.
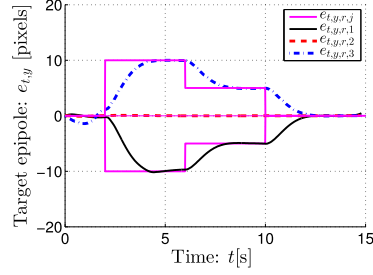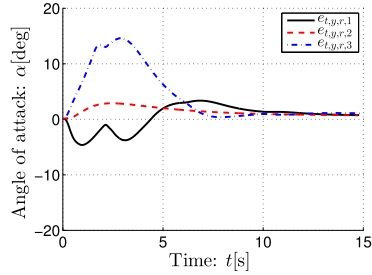
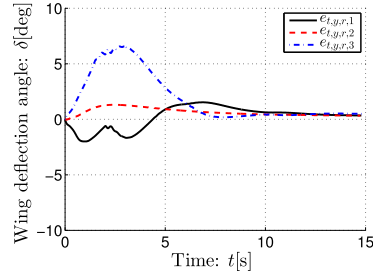(a) Trajectory

(b) Lateral acceleration: n

(c) Current epipolar coordinate: $e_{c,y}$

(d) Target epipolar coordinate: $e_{t,y}$

(e) Angle of attack: α

(f) Wing deflection angle: δ

Fig. 8 Interception of a target camera.

Figure 8(a) shows the trajectories followed by the vehicle. Given that the end values of each reference are zero (Fig. 8(d)), conditions of Corollary 1 are satisfied, so, the interception of the target camera is ensured. It is observed in Fig. 8(b) that a larger acceleration is required when the vehicle starts to move with a high initial orientation. Since the vehicle has no propulsion it has flight against the gravity. Fig. 8(e) and Fig. 8(f) show that α and δ stay under reasonable bounds avoiding the system become unstable.

2. LoS angle control

This experiment shows how a control of the LoS angle, λ, is achieved when the vehicle follows three different target epipolar references. Each reference is defined as $\xi_{t,1,r,j} = e_{t,y,r,j} = S_j[u_s(t-1-j) + u_s(t-5-j)]$ pixels, with $j = 1, 2, 3$, $S_1 = -2$, $S_2 = -6$, and $S_3 = -16$. The current camera, C, has the initial conditions: ${}^{\mathcal{A}}\mathbf{c}_0 = {}^{\mathcal{A}}[0, 0, h_0]^T$ m, ${}^{\mathcal{B}}\mathbf{v}_{c,0} = {}^{\mathcal{B}}[240, 0, 0]^T$ m/s, and $\gamma_{c,0} = 45$ deg. Fig. 9 shows the experiment results.

(a) Trajectory

(b) Target epipolar coordinate: $e_{t,y}$

(c) LoS angle: λ

(d) Lateral acceleration: n

(e) Angle of attack: α

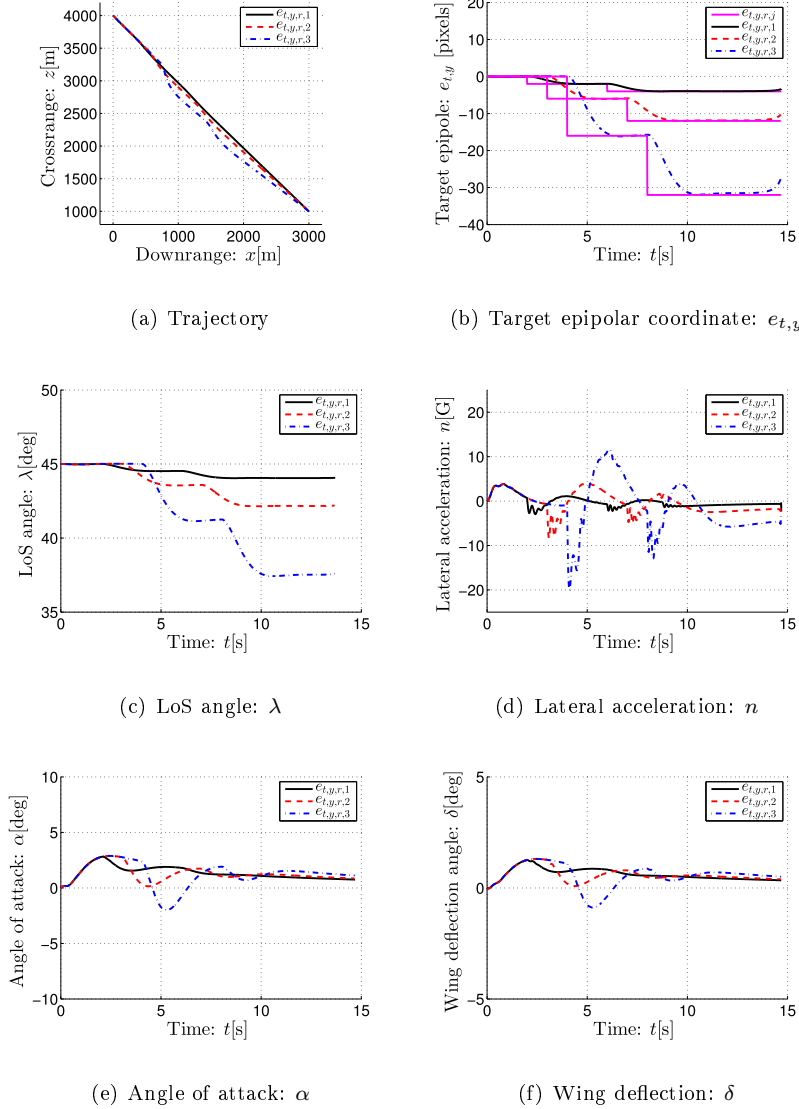(f) Wing deflection: δ

Fig. 9 LoS angle control.

Figure 9(a) shows the trajectories followed for the vehicle. Since conditions of Corollary 1 are satisfied, every current camera intercepts the target camera. Fig. 9(b) shows the tracking of target

epipolar reference, and Fig. 9(c) shows the stabilization of λ to a values that are defined by the target epipolar references. The final LoS angles obtained in this experiment are 44.05 deg, 42.14 deg, and 37.41 deg, in accordance with Eq. (28). In Fig. 9(d), Fig. 9(e), and Fig. 9(f), we observe that the current camera following the larger epipolar reference ($S_3 = -16$) requires the larger values of n, α, and δ. However, vehicle's aerodynamic properties are not exceeded.

E. Noise Sensitivity Analysis

The most influential variables in the behavior of the proposed guidance strategies are: the initial vehicle attitude θ_0, the flight-path angle γ_c, and the epipolar coordinates measurements, $e_{c,y}$ and $e_{t,y}$. Therefore, a set of Monte-Carlo simulations with noise added to the referred variables have been proposed to show the performance of the guidance strategies.

The simulations were conducted for the case of interception of the target camera position. The initial conditions were set to: $\xi_{c,1,r} = e_{c,y,r} = 0$ pixels, $^{\mathcal{A}}\mathbf{c}_0 = {}^{\mathcal{A}}[0, 0, h_0]^T$ m, $^{\mathcal{B}}\mathbf{v}_{c,0} = {}^{\mathcal{B}}[195, 0, 0]^T$ m/s, and $\theta_0 = \gamma_{c,0} = 45$ deg, for the CEBG, and $\xi_{t,1,r} = e_{t,y,r} = 0$ pixels, $^{\mathcal{A}}\mathbf{c}_0 = {}^{\mathcal{A}}[0, 0, h_0]^T$ m, $^{\mathcal{B}}\mathbf{v}_{c,0} = {}^{\mathcal{B}}[240, 0, 0]$ m/s, and $\theta_0 = \gamma_{c,0} = 45$ deg, for the TEBG. We have chosen the same values for $^{\mathcal{A}}\mathbf{a}$, $^{\mathcal{A}}\mathbf{t}$, γ_t, and $\mathbf{K}_t$, than those specified in Sec. IV.C and Sec. IV.D.

The following noise sources have been chosen to make the simulations: $N_1 = \theta_0 + U(-2, 2)$ (deg), $N_2 = \gamma_c + U(-0.1, 0.1)$ (deg), and $N_3 = \{e_{c,y} + U(-10, 10), e_{t,y} + U(-10, 10)\}$ (pixels,pixels). $U(a, b)$ is an uniform noise defined in the interval (a, b). The selected intervals allow successful (stable) simulations. A total of 100 runs were analyzed for each strategy and the results of the simulations are presented in Fig. 10 and Table 1.

For the CEBG: Fig. 10(a), Fig. 10(c), and Fig. 10(e) show the noisy final positions (red plus signs) for each run and the ideal final position located at $(2678, 1307)$ m at time 15.66 s (blue asterisk). According to these figures, the noisy final positions approximately move along of a straight line and we can say that, even though noise is added to the variables, eventually the target position can be reached at another time.

For the TEBG: Fig. 10(b), Fig. 10(d), and Fig. 10(f) show the noisy final positions and the ideal final position located at $(2650, 1350)$ m at time 13.25 s. Also, for this strategy, we can say

(a) CEBG: N_1

(b) TEBG: N_1

(c) CEBG: N_1 and N_2

(d) TEBG: N_1 and N_2

(e) CEBG: N_1, N_2, and N_3
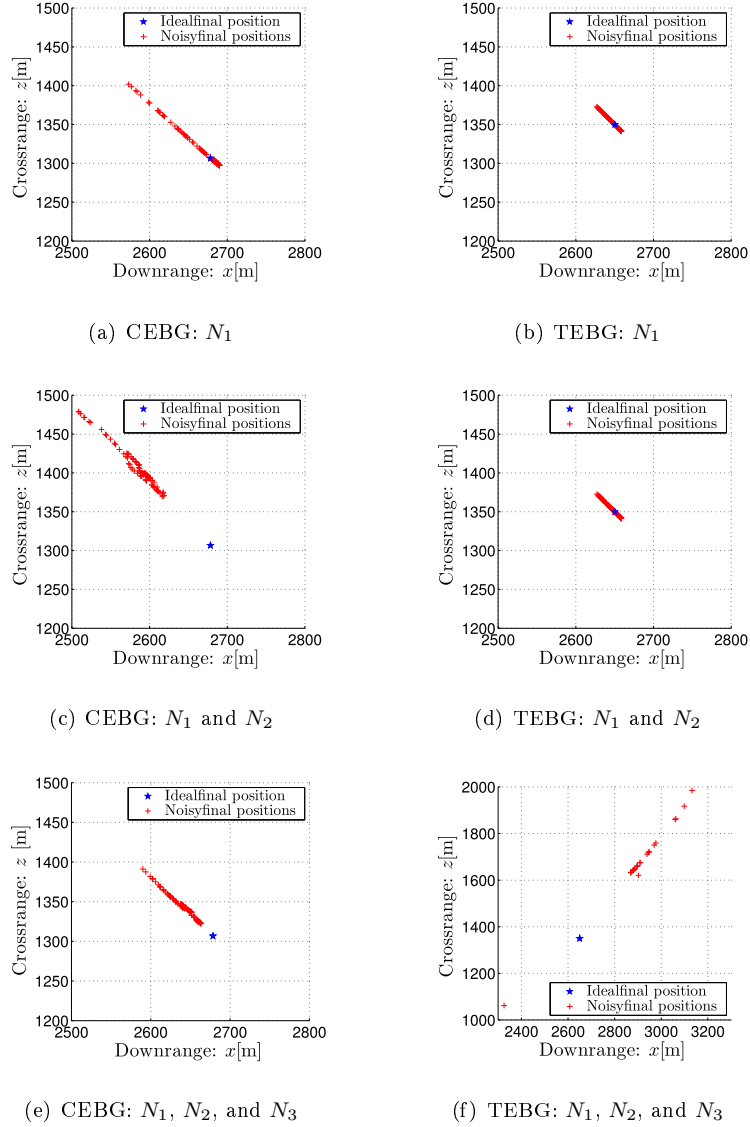
(f) TEBG: N_1, N_2, and N_3

Fig. 10 Final positions for Monte-Carlo simulations for interception of a target camera.

that even though noise is added to the variables, eventually, the target position can be reached at another time, except for the case when noise is added to the target epipole $e_{t,y}$ (Fig. 10(f)). In this case, the reference of the strategy is changed through the flight time and the guidance algorithm tries to follow it. If this reference is changed, the goal of interception cannot be achieved.

Table 1 shows the mean values of the components in x and y of the position errors (μ_x and μ_y) and the standard deviations (σ_x and σ_y) in the final positions achieved by the guidance strategies. For the noise N_1 and N_2, it can be concluded that the TEBG has better performance than the CEBG since final position errors are low. However, high noise values over the target epipolar coordinate,

included in N_3, are not admissible for the purpose of interception of the target camera by the TEBG algorithm. Fig. 10(e) shows that the same noise, N_3, can be handled by the CEBG algorithm.

Table 1 Monte-Carlo simulations results for interception of a target camera

Noise	CEBG				TEBG			
	μ_x (m)	μ_y (m)	σ_x (m)	σ_y (m)	μ_x (m)	μ_y (m)	σ_x (m)	σ_y (m)
N_1	22.8	20.0	25.6	25.6	7.94	7.93	5.73	5.73
N_1 and N_2	94.4	99.9	26.6	26.6	8.29	8.27	5.96	5.96
N_1, N_2, and N_3	39.6	38.4	18.0	18.0	518	749	242	242

We can say that the guidance algorithms can lead the current camera to the target camera position, under appropriate noise levels, but with time delay and a position error that depends on the noise power. These results can be expected given the conditions established for Corollary 1 and Corollary 2. On the other hand, we can say that suddenly perturbations on airframe's stability, and/or camera orientations, and/or epipole estimation errors, can make the features leave the FoV of the current camera. In this case, the guidance algorithms will require additional strategies to deal with this problem. This topic has been studied for several authors [20-23], and its study over the CEBG and TEBG algorithms is not in the scope on this paper.

V. Conclusion

We have developed two strategies based on epipolar geometry to guide an autonomous glider to a desired position. Their performances are shown by simulations over a specific type of aerial vehicle.

The target epipole-based guidance (TEBG) is independent of the current camera angular acceleration, $\ddot{\gamma}_c$. Then, the stability of the origin of the full closed-loop system is always ensured and it is asymptotically stable. Whereas, for the current epipole-based guidance (CEBG), the angular velocity, $\dot{\gamma}_c$, should be zero in order to achieve stability. If $\dot{\gamma}_c$ is not a vanishing perturbation, and in presence of an additional perturbation, ω_i, only ultimately boundedness can be ensured for both strategies and under the conditions explained in Corollary 2.

Even though the aerial vehicle that was used here has not an equilibrium point, the goal of the

guidance of the current camera to a desired target camera position is achieved with both guidance methods. This was possible because the initial conditions of the guidance experiments avoid the vehicle enters into instability. In addition, the lead angle and the LoS angle can be stabilized by the CEBG and TEBG, respectively. Also, Monte-Carlo simulations with noise added to the relevant variables, that can lead the system to instability, have been done to shown the performance of both guidance algorithms. The advantages of each strategy have been showed by ideal and noisy simulations.

The main contribution of the proposed guidance strategies is their independence of the range magnitude, $r_{c,t}$, and its rate of change, $\dot{r}_{c,t}$, since these variables have been removed completely by the input-output linearization technique. The two presented guidance strategies can be studied for extrapolation to a different kind of aerial vehicle; however, to ensure successful outcomes, it is required analysis of stability and performance of the selected autopilot according to the limits of the airframe's aerodynamic capabilities and the initial conditions that will be chosen.

Appendix

A.   Proof of Corollary 1

Firstly, we can see that if $\dot{\gamma}_i$ is a vanishing perturbation, then $\dot{\gamma}_i$ and $\ddot{\gamma}_i$ will be equal to zero for all $t > t_d$ ($t_d > 0$). Thus, the path angle γ_i will be a constant value and, if $\omega_i = 0$, the perturbation W_i, defined in Eq. (27), will be equal to zero for all $t > t_d$. Under these conditions, and from Eq. (25), the nonperturbed full closed-loop system will be

$$\dot{\chi}_i = f(\chi_i) \quad . \tag{35}$$

Next, to find the equilibrium $\chi_{i,ss}$ of Eq. (35), we do $f(\chi_{i,ss}) = 0$, and, using Eq. (18) and Eq. (24) in Eq. (25), and after some algebra, it results that

$$0 = \eta_{2,ss}$$

$$0 = \xi_{i,2,ss}$$

$$0 = -k_{i,1}\xi_{i,1,ss} - k_{i,2}\xi_{i,2,ss} - k_{i,3}\sigma_{i,ss} \tag{36}$$

$$0 = -\xi_{i,1,ss} + \xi_{i,1,r} \quad .$$

At the equilibrium, and taking Eq. (6a) and Eq. (6b) into account, we can see that $\eta_{1,ss} = \gamma_i + m_i$, where $m_i = \arctan(\xi_{i,1,r}/f_i)$. Therefore, and from Eq. (36), the nonperturbed full closed-loop system in Eq. (35) has the equilibrium subspace

$$\chi_{i,ss} = \left[\gamma_i + m_i, \ 0, \ \xi_{i,1,r}, \ 0, \ -\frac{k_{i,1}}{k_{i,3}}\xi_{i,1,r}\right]^T \quad . \tag{37}$$

Now, to prove the stability of this equilibrium, we analyze the stability of the origin (because a change of variables in the original system can shift any equilibrium point to the origin). In Eq. (37), we can see that if the epipolar coordinate reference is set to zero, $\xi_{i,1,r} = 0$, then the equilibrium becomes the origin $\chi_{i,ss} = \mathbf{0}$.

From Theorem 4.5 in [30], we can say that since the matrix $\mathbf{A}_{i,a}$ is Hurtwitz, i.e., all its eigenvalues have negative real part, then the equilibrium $\mathbf{x}_{i,ss} = \mathbf{0}$ is asymptotically stable (moreover, it is exponentially stable). That means that, for each $\varepsilon > 0$, there is a $\delta = \delta(\varepsilon) > 0$ such that $\|\mathbf{x}_i(0)\| < \delta(\varepsilon)$ and $\lim_{t\to\infty} \mathbf{x}_i = \mathbf{0}$. $\|\cdot\|$ is a norm. In addition, and for each controller, since the epipolar coordinates are related to the η-state by Eq. (6a) and Eq. (6b), we can verify that the η-trajectory satisfy, for all $t > t_d$, the following statements:

- For the CEBG, since $\eta_1 = \arctan(\xi_{c,1}/f_c)$, with $m_c = 0$ and $\dot{\gamma}_c = 0$, and $\eta_2 = \dot{\eta}_1 = (f_c^2\xi_{c,2})/(\xi_{c,2}^2 + f_c^2)$, then $\lim_{\|\mathbf{x}_i\|\to 0} \eta_1 = 0$ and $\lim_{\|\mathbf{x}_i\|\to 0} \eta_2 = 0$.

- For the TEBG, since $\eta_1 = -\arctan(\xi_{t,1}/f_t)$, with $m_t = 0$ and $\dot{\gamma}_t = 0$, and $\eta_2 = \dot{\eta}_1 = -(f_t^2\xi_{t,2})/(\xi_{t,2}^2 + f_t^2)$, then $\lim_{\|\mathbf{x}_i\|\to 0} \eta_1 = 0$ and $\lim_{\|\mathbf{x}_i\|\to 0} \eta_2 = 0$.

Finally, with the above findings, we can conclude that, for each $\varepsilon > 0$, there is a $\delta = \delta(\varepsilon) > 0$ such that $\|\chi_i(0)\| < \delta$ and $\lim_{t\to\infty} \chi_i = \mathbf{0}$ for all $t > t_d$. Then, the origin, $\chi_{i,ss} = \mathbf{0}$, of the

non-perturbed system in Eq. (35) is asymptotically stable for all $t > t_d$. The same result could be achieved by Lemma 13.1 in [30], where the full closed-loop system is viewed as a cascade system and when the $\mathbf{x}_i$-state acts as the input of the η-system.

B.   Proof of Corollary 2

To prove the first part of this corollary we can say, as in the proof of the Corollary 1, that if both perturbations, ω_i and $\dot{\gamma}_i$, are vanishing for all $t > t_d$ ($t_d > 0$), then W_i, in Eq. (27), will be equal to zero, and the full closed-loop system, in Eq. (25), will be $f(\chi_i)$. The equilibrium of this nonperturbed system is the same equilibrium displayed by Eq. (37), and asymptotically stability of the origin, $\chi_{i,ss} = \mathbf{0}$, can be proved by Corollary 1.

To prove the second part, we can say that if the perturbation $\omega_i \neq 0$ for all t, then the full closed-loop system, in Eq. (25), has no longer an equilibrium (η-state is not controllable). Consequently, we only can expect, for all $t > t_d$, that the χ_i-trajectories will be ultimately bounded. First, we focus on the subsystem $\dot{\mathbf{x}}_i$, and if the perturbation ω_i meets

$$\|\omega_i\| \leq k\|\mathbf{x}_i\| \quad , \tag{38}$$

for all $\mathbf{x}_i$, with $k < 1/(2\|\mathbf{P}_i\mathbf{B}_{i,a}\|)$, and $\mathbf{P}_i = \mathbf{P}_i^T$ is a positive definite matrix that is the unique solution of the Lyapunov equation $\mathbf{P}_i\mathbf{A}_{i,a} + \mathbf{A}_{i,a}^T\mathbf{P}_i = -\mathbf{I}$ (because $\mathbf{A}_{i,a}$ is Hurwitz, Theorem 4.6 in [30]), then, by Lemma 13.3 in [30], the origin $\mathbf{x}_{i,ss} = \mathbf{0}$ will be globally exponentially stable. This means that $\|\mathbf{x}_i\| = 0$ as $t \to \infty$ and, since $\dot{\gamma}_i$ is equal to zero for all $t > t_d$, then, from Eq. (26) and Eq. (27), we will have that $\dot{\eta}_2 = \omega_i/f_i$, i.e., the perturbation is weighted by f_i. Next, and from Lemma 9.3 in [30], we can say that due to the origin of the nonperturbed system, $f(\chi_i)$ with $\omega_i = 0$, is asymptotically stable (by Corollary 1), and assuming that the perturbation satisfies

$$\|\omega_i\| \leq f_i w_1 < f_i w_2(l_1) \quad , \tag{39}$$

where w_1 is a parameter that is bounded by the function $w_2(l)$, which in turns is a function that is composed of a set of class $\mathcal{K}$ functions. Then, the trajectories of the perturbed full closed-loop

system, in Eq. (25), satisfy

$$\|\chi_i\| \le w_3(\|\chi_i(t_0)\|, t - t_0) \quad , \quad \forall \quad t_0 \le t < t_0 + T_1 \quad , \tag{40}$$

and

$$\|\chi_i\| \le w_4(w_1) \quad , \quad \forall \quad t \ge t_0 + T_1 \quad , \tag{41}$$

where $t_0 \ge t_d$, T_1 is some finite time, w_3 is a class $\mathcal{KL}$ function, and w_4 is a class $\mathcal{K}$ function that depends on w_1. According to Lemma 9.3 in [30], the specific form of w_2, w_3, and w_4 will depend on the Lyapunov function, $V(\chi_i)$, that could be defined in a domain $D = \{\chi_i \in \mathbb{R}^5 \mid \|\chi_i\| < l_1\}$ (l_1 is the radious of the ball). Finally, and putting together the requirements of Lemmas 9.3 and 13.3 in [30], and taking Eq. (38) and Eq. (41) into account, we can say that the χ_i-trajectories will be ultimately bounded, for all $t > t_0 + T_1$, if the following bound for the perturbation ω_i is fulfill,

$$\|\omega_i\| \le k\|\mathbf{x}_i\| \le k\|\chi_i\| \le kw_4(w_1) \quad . \tag{42}$$

The proof of the third part of the corollary is similar to the proof of the second part. Here, we only emphasize that the condition for Lemma 9.3 in [30] is $\|\omega_i/f_i + \ddot{\gamma}_i\| \le w_5 < w_6(l_2)$, where w_5 is a parameter that is bounded by the function $w_6(l_2)$. $w_6(l_2)$ is a function composed of a set of class $\mathcal{K}$ functions and l_2 is the radius of the ball, or the domain of a Lyapunov function for the full system.

References

[1] Schneiderman, R., "Unmanned Drones are Flying High in the Military/Aerospace Sector [Special Reports]," *IEEE Signal Processing Magazine*, Vol. 29, No. 1, Jan. 2012, pp. 8-11.

doi: 10.1109/MSP.2011.943127

[2] Wilson, J. R., "UAV Roundup 2013," *AIAA Aerospace America*, Vol. 51, No. 7, Jul. 2013, pp. 26-36.

[3] Werner, D., "Making Way for Unmanned Aircraft," *AIAA Aerospace America*, Vol. 52, No. 1, Jan. 2014, pp. 28-31.

[4] Hutchinson, S., Hager, G. D., and Corke, P. I., "A Tutorial on Visual Servo Control," *IEEE Transactions on Robotics and Automation*, Vol. 12, No. 5, Oct. 1996, pp. 651-670.

doi: 10.1109/70.538972

[5] Chaumette, F., and Hutchinson, S., "Visual Servo Control. II. Advanced Approaches [Tutorial]," *IEEE Robotics Automation Magazine*, Vol. 14, No. 1, March. 2007, pp. 109-118.

doi: 10.1109/MRA.2007.339609

[6] Rives, P., "Visual Servoing Based on Epipolar Geometry," *IEEE/RSJ International Conference on Intelligent Robots and Systems, 2000. (IROS 2000). Proceedings.*, Vol. 1, 2000, pp. 602-607.

doi: 10.1109/IROS.2000.894670

[7] Mariottini, G.L., Prattichizzo, D., and Oriolo, G., "Epipole-based visual servoing for nonholonomic mobile robots," *IEEE International Conference on Robotics and Automation, 2004. ICRA '04. Proceedings.*, Vol. 1, Apr. 2004, pp. 497-503.

doi: 10.1109/ROBOT.2004.1307198

[8] Mariottini, G.L., Oriolo, G., and Prattichizzo, D., "Image-Based Visual Servoing for Nonholonomic Mobile Robots Using Epipolar Geometry," *IEEE Transactions on Robotics.*, Vol. 23, No. 1, Feb. 2007, pp. 87-100.

doi: 10.1109/TRO.2006.886842

[9] López-Nicolás, G., Sagüés, C., Guerrero, J.J., Kragic, D., and Jensfelt, P., "Nonholonomic Epipolar Visual Servoing," *IEEE International Conference on Robotics and Automation, 2006. ICRA '06. Proceedings.*, May. 2006, pp. 2378-2384.

doi: 10.1109/ROBOT.2006.1642058

[10] López-Nicolás, G., Sagüés, C., Guerrero, J.J., Kragic, D., and Jensfelt, P., "Switching Visual Control Based on Epipoles for Mobile Robots," *Robotics ans Autonomous Systems*, Vol. 56, No. 7, 2008, pp. 592-603.

doi: 10.1016/j.robot.2007.10.005

[11] López-Nicolás, G., Guerrero, J.J., and Sagüés, C., "Visual Control of Vehicles Using Two-View Geometry," *Mechatronics*, Vol. 20, No. 2, 2010, pp. 315-325.

doi: 10.1016/j.mechatronics.2010.01.005

[12] Gurfil, P., and Rotstein, H., "Partial Aircraft State Estimation from Visual Motion Using the Subspace Constraints Approach," *Journal of Guidance, Control, and Dynamics*, Vol. 24, No. 5, Sept. 2001, pp. 1016-1028.

doi: 10.2514/2.4811

[13] Indelman, V., Gurfil, P., Rivlin, E., and Rotstein, H., "Distributed Vision-Aided Cooperative Localization and Navigation Based on Three-View Geometry," *Robotics and Autonomous Systems*, Vol. 60, No. 6, June 2012, pp. 822-840.

doi: 10.1016/j.robot.2012.02.003

[14] Indelman, V., Gurfil, P., Rivlin, E., and Rotstein, H., "Real-Time Vision-Aided Localization and Navigation Based on Three-View Geometry," *IEEE Transactions on Aerospace and Electronic Systems*, Vol. 48, No. 3, July 2012, pp. 2239-2259.

doi: 10.1109/TAES.2012.6237590

[15] Webb, T.P., Prazenica, R.J., Kurdila, A.J., and Lind, R., "Vision-Based State Estimation for Autonomous Micro Air Vehicles," *Journal of Guidance, Control, and Dynamics*, Vol. 30, No. 3, May 2007, pp. 816-826.

doi: 10.2514/1.22398

[16] Koch, A., Wittig, H., and Thielecke, F., "A Vision-Based Navigation Algorithm for a VTOL- UAV," AIAA Guidance, Navigation, and Control Conference and Exhibit, AIAA Paper 2006-6546, Aug. 2006.

doi:10.2514/6.2006-6546

[17] Johnson, E. N., Calise, A. J., Watanabe, Y., Ha, J., and Neidhoefer, J. C., "Real-Time Vision-Based Relative Aircraft Navigation," *Journal of Aerospace Computing, Information, and Communication*, Vol. 4, No. 4, Apr. 2007, pp. 707-738.

doi: 10.2514/1.23410

[18] Ma, L., Cao, C., Hovakimyan, N., Woolsey, C., Dobrokhodov, V., and Kaminer, I., "Development of a Vision-Based Guidance Law for Tracking a Moving Target," AIAA Guidance, Navigation, and Control Conference and Exhibit, AIAA Paper 2007-6744, Aug. 2007.

doi: 10.2514/6.2007-6744

[19] Ma, L., Cao, C., Hovakimyan, N., Woolsey, C., Dobrokhodov, V., and Kaminer, I., "Adaptive Vision-Based Guidance Law with Guaranteed Performance Bounds," *Journal of Guidance, Control, and Dy-*

namics, Vol. 33, No. 3, May 2010, pp. 834-852.

doi: 10.2514/1.46287

[20] Martínez, J., Hernández, J., and Rodríguez, C., "A Vision Based Algorithm for the Guidance of a Glider," *Workshops of SIBGRAPI (2013)*, Arequipa, Perú, Aug. 2013.

[21] Kaiser, M.K., Gans, N.R., and Dixon, W.E., "Vision-Based Estimation for Guidance, Navigation, and Control of an Aerial Vehicle," *IEEE Transactions on Aerospace and Electronic Systems*, Vol. 46, No. 3, July 2010, pp. 1064-1077.

doi: 10.1109/TAES.2010.5545174

[22] Dupree, K., Gans, N.R., MacKunis, W., and Dixon, W.E., "Euclidean Calculation of Feature Points of a Rotating Satellite: A Daisy-Chaining Approach," *Journal of Guidance, Control, and Dynamics*, Vol. 31, No. 4, July 2008, pp. 954-961.

doi:10.2514/1.33087

[23] Lee, D., Lim, H., Kim, H. J., Kim, Y., and Seong, K. J., "Adaptive Image-Based Visual Servoing for an Underactuated Quadrotor System," *Journal of Guidance, Control, and Dynamics*, Vol. 35, No. 4, July 2012, pp. 1335-1353.

doi: 10.2514/1.52169

[24] Achicanoy, W., Sagüés, C., López-Nicolás, G., and Rodríguez, C., "Two-view Epipole-based Guidance Control for Autonomous Unmanned Aerial Vehicles," *Proceedings of ICINCO*, Vol. 2, 2012, pp. 242-248.

doi: 10.5220/0004032402420248

[25] Hartley, R. I., and Zisserman, A., *Multiple View Geometry in Computer Vision*, 2nd ed., Cambridge University Press, Cambridge, 2004, Chaps. 9, 11.

[26] Shneydor, N. A., *Missile Guidance and Pursuit: Kinematics, Dynamics and Control*, 1st, ed., Woodhead Publishing Limited, 1998, Chaps. 1, 2, 3.

[27] Chen, C. T., *Linear System Theory and Design*, 3rd, ed., Oxford University Press, 1998, Chaps. 8, 9.

[28] Yanushevsky, R., "Parallel Navigation," *Modern Missile Guidance*, 1st ed., CRC Press, Boca Raton, 2007, pp. 9-19.

[29] Siouris, G. M., *Missile Guidance and Control Systems*, 1st ed., Springer, 2004, Chaps. 2, 3.

[30] Khalil, H. K., *Nonlinear Systems*, 3rd ed., Prentice Hall, Upper Saddle River, NJ, 2002, Chaps. 4, 9, 12, 13.

[31] Chin, S. S., *Missile Configuration Design*, 1st ed., McGraw-Hill, 1961.

[32] Melin, T., "TORNADO: a Vortex–Lattice MATLAB Implementation for Linear Aerodynamic Wing Applications," Master Thesis, Royal Insitute of Technology (KTH), Department of Aeronautics, Sweden,

2000.

[33] Zarchan, P., *Tactical and Strategic Missile Guidance*, 5$^\text{th}$ ed., AIAA, 2007.